CHAPTER 2

Design for improved energy absorption of the frames fabricated from graphite-epoxy tape

Semi-circular, I-section frames fabricated from graphite/epoxy unidirectional tape, available from an earlier study by Moas (1996), are redesigned for improved energy absorption using the computer code OPTFAIL, developed by Woodson (1994). Designing these existing frames is limited to reducing the widths of the flanges around the circumference. In spite of this limited design flexibility, it is important to assess the methodology underlying Woodson's code. Hence, a series of static tests of the redesigned frames is conducted and the results of those tests are discussed in this chapter. In Section 2.1, the optimal design methodology used in Woodson's code is reviewed. In Section 2.2 the analysis module of Woodson's code is used to predict the response of one of the I-section frames tested by Moas, and the correlation of the analysis and test results serves as a baseline case. With confidence in the analysis established from the baseline case, the design of the frame specimens is described in Section 2.3. The test apparatus and procedure for the tests of the frames redesigned for improved energy absorption are described in Section 2.4, and the test results are discussed in Section 2.5. Finally, a comparison between analysis and tests is presented in Section 2.6.

2.1 Optimal design methodology for energy absorption

The design to maximize the energy absorbed by the structure subject to a constraint on the maximum load is performed in an effort to attain the ideal response of a controlled failure

load followed by a sustained crushing force. The maximum failure load constraint is prescribed because the accelerations in a crash event are directly related to the load, and accelerations need to be limited for passenger survival. The mathematical statement of the optimization problem is

$$\begin{aligned} &\text{maximize} \quad E_a = \int_0^{\delta_{ult}} F(\delta, \hat{x})\, d\delta \\ &\text{subject to} \quad F \le F_{max} \end{aligned} \tag{2.1}$$

where E_a denotes the energy absorbed, F the contact force, d the contact displacement, $\hat{x}$ the vector of design variables, and F_{max} denotes the maximum value of the contact force. The upper limit, d_{ult}, in Eq. (2.1) denotes the ultimate displacement which we specify to be the value of the displacement d where failure causes a 25% reduction in the contact force F. In the analysis the contact displacement is specified and the value of the contact force is computed from the response. The design variables can include the laminate stacking sequence and dimensions of the cross section. However, since we are redesigning existing frames in this work, only the dimensions of the cross section are used as design variables. The computer code developed by Woodson et al. (1996) is used for the optimization. This code was developed to optimize open section curved composite frames for crashworthiness under static loading. A genetic algorithm is used for the optimization, a curved beam finite element analysis based on a Vlasov-type thin walled bar theory is used for the structural response (Woodson et al., 1993), and the selective and progressive ply-by-ply degradation model for graphite-epoxy laminates (Tsai, 1992) is implemented as the failure model.

A genetic algorithm is selected for the optimization because the objective and constraint functions are discontinuous in the design variables and the design variables are discrete. The objective function is discontinuous in the design variables because the location of failure can suddenly change with the design changes. Also, for manufacturing considerations we limit the ply angles and the sizing variables to discrete values. Hence, the use of a gradient based algorithm is difficult. In addition, gradient based algorithms usually locate the nearest local optimum which may not be the global optimum, so that several dif-

ferent initial designs must be considered. The genetic algorithm is a probabilistic method based on Darwin's principle of survival of the fittest, and does not require computation of sensitivity derivatives. In biological populations, individual characteristics are stored as chromosomal strings, and for artificial systems the design variables representing the individual design are encoded as numerical strings. Each gene in the chromosomal string can take on prescribed values or alleles. A population of designs evolves from one generation to the next by mimicking the biological processes of reproduction and mutation. Reproduction is represented by the crossover operator which is the exchange of genetic information between the chromosomal strings of the parents. Crossover and mutation are the basic operators that result in a structured yet randomized exchange of genetic information. The fittest individuals (designs) are more likely to breed and pass on good traits to the succeeding generation. The fact that many designs are considered simultaneously, implies that achieving a globally optimal design is more likely than with algorithms that consider only the evolution of one design. The fitness function used to assess the merits of a given frame design is defined by

$$\begin{aligned} f &= E_a \qquad F \le F_{max} \\ f &= E_a - (pg + \bar{\delta}) \qquad F > F_{max} \end{aligned} \tag{2.2}$$

in which the two parameters p and $\bar{\delta}$ are used to penalize infeasible designs, and the constraint violation g is defined by

$$\begin{aligned} g &= \int_0^{\delta_{ult}} F(\delta) U[F(\delta) - F_{max}] d\delta \\ U[\bullet] &= \begin{pmatrix} 1, [\bullet] > 0 \\ 0, [\bullet] < 0 \end{pmatrix} \end{aligned} \tag{2.3}$$

The values selected for the penalty parameters are p = 1.25 and $\bar{\delta}$ = 25 lb-in. A fixed population size of ten designs, a single point crossover with a rate of 75%, a mutation rate of 15%, an elitist strategy (the best individual in a generation is cloned to the next generation), and a no-twins rule (each individual design in a generation is unique) were used. Convergence of the algorithm was defined as no improvement in the designs after 25 gen-

erations. Examples of the application of genetic algorithms to structural optimization can be found in the work by Hajela (1990), Lin and Hajela (1992), Le Riche and Haftka (1993), and Gürdal et al. (1994).

A genetic algorithm requires many analyses to be performed, so that traditional crash analysis via computer programs like DYNA3D (Hallquist and Benson, 1986) or DYCAST (Pifko et al., 1987) are too expensive to incorporate in optimization. Instead, a Vlasov-type composite curved beam analysis is used for the response of the frame (Woodson et al., 1993). The Vlasov theory for straight beams with homogeneous, isotropic, thin-walled construction as presented by Gjelsvik (1981) is extended to curved beams with laminated composite wall construction by Woodson et al. (1993). Vlasov theory is a generalization of Bernoulli-Euler beam theory in which the shear strain is assumed to vanish only at the reference surface of each branch of the cross section. The shear strain of parallel surfaces of each branch is non-zero and accounts for improved torsional response of the thin-walled bar theory over conventional beam theory. The curved beam analysis was compared to a branched shell finite element analysis by Woodson et al. (1993) to determine its limitations. For the laminated wall constructions and cross-sectional dimensions used in this study the curved beam analysis should give reasonably accurate results.

The selective and progressive ply-by-ply degradation model for brittle failure of laminated composites developed by Tsai (1992) is used for the material degradation model. Each lamina is examined for failure initiation, and those laminae predicted to fail have selected material properties degraded either in a matrix mode or a fiber mode. The stiffness of the degraded laminate is recomputed using Classical Lamination Theory (CLT) and analyzed again for failure. This process continues until all laminae have failed in a fiber mode. The laminate progressive failure model results in a sequence of linear analyses, with each subsequent analysis in the sequence having a greater reduction in laminate stiffness. An evaluation of this method for progressive failure analysis is conducted by comparing the analysis results to the available data from a limited number of test cases (Woodson et al., 1996).

2.2 Correlation of the analysis to the baseline frame test

Four of the fifteen frames listed in Table 1.1 are available from the earlier test program (Moas et al., 1994), and these are labeled as FR002I-1, FR004I-1, FR005I-2, FR006I-2. These frame specimens are denoted here in an abbreviated notation as 2I-1, 4I-1, 5I-2, and 6I-2, respectively. The frames are fabricated from AS4/5208 graphite-epoxy unidirectional tape. Frames 2I-1 and 2I-3 are nominally the same, and 2I-3 was tested by Moas et al. (1994) (denoted in that reference as Frame #2). Hence, frame 2I-3 is selected as the baseline case and frames 2I-1, 5I-2, and 6I-2 as the ones to be optimized. The load-displacement response of frame 2I-3 measured during the test is shown in Fig. 2.1 as the solid line. The analysis module of the optimization code (OPTFAIL: Woodson, 1994) is used to predict the load-displacement response of this baseline frame. Measured dimensional data listed in Table 1.2, and the nominal material properties listed in column five of Table 2.1 (labeled Woodson), are used in the analysis. Two analytical predictions of the response are shown in Fig. 2.1: in one case fully clamped end conditions are specified, and in the other case hinged end conditions are specified for the rotation in the plane of the frame.

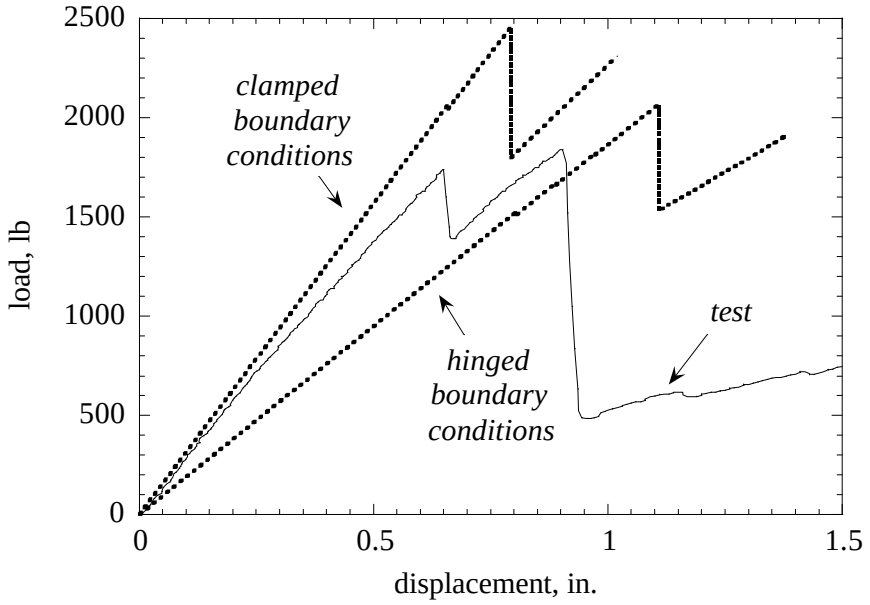

Fig. 2.1 Analytical results for clamped and hinged boundary conditions.

As can be seen from Fig. 2.1, the initial slope of the load-displacement response from the test falls between the slopes predicted from the two analyses, with the slope from the clamped end analysis closer to test result. However, actual end conditions are neither clamped or hinged but elastic. Elastic end conditions are not modeled in the analysis. Also, the maximum loads predicted by the analyses exceed the experimental failure load. For clamped boundary conditions the maximum load is about 2500 lb, for hinged ends it is about 2000 lbs, and the maximum load from the test is about 1800 lb.

To improve the correlation of the analysis to the test results for the baseline frame, a sensitivity study is performed to evaluate the influence of material property changes on the load-displacement response. First, the influence of the fiber volume fraction is considered. The nominal value given for this material is 60% ± 5%. Using the rule of mixtures, changes in the lamina stiffness properties (E_1, E_2, G_{12}, n_{12}) about the nominal values listed in the fifth column (labeled Woodson) of Table 2.1 are computed. Only small differ-

Table 2.1 AS4/XXXX graphite-epoxy tape material properties.

	Sensmeier (1988)	**Collins (1991)**	**Tsai (1992)**	**Woodson (1994)**	**Moas (1996)**	**selected values**
material	AS4/3502	AS4/5208	AS4/35XX	AS4/5208	AS4/5208	AS4/5208
E_1, Msi	14.56-24.72	18.4	---	18.4	18.4	17.0
E_2, Msi	0.760-1.48	1.64	---	1.64	1.64	1.64
G_{12}, Msi	0.420-0.820	0.870	---	0.870	0.870	0.611
n_{12}	0.290	0.300	0.270	0.300	0.300	0.300
X, Ksi	167.4-182.5	---	209.9	197.9	178.1	167.4
X', Ksi	121.6-139.0	---	209.9	160.0	132.4	121.6
Y, Ksi	7.42-7.51	---	7.5	5.50	7.46	7.42
Y', Ksi	30.4-33.6	---	29.9	29.9	32.3	30.4
S, Ksi	11.9-13.1	---	13.4	14.0	12.5	14.0
F_{12}^*	---	---	---	-0.5	---	-0.5
V_f	---	---	---	0.600	0.600	0.600
t, in.	---	0.00550	---	0.00500	0.00500	0.00500

ences in the load-displacement response curves for values of the fiber volume fraction of 55% and 65% are found. Second, the nominal material properties given by Moas (1996), listed in column six of Table 2.1, are used in the analysis. The moduli used by Moas are the same as those used by Woodson (1994), but Moas used lower strength values. Since the material degradation model is dependent on the five basic strength values (X, X', Y, Y', S) of the lamina, it is expected that the initial values for these strengths will influence the load-displacement response. Using the material properties from Moas (1996), it is found that the response is particularly sensitive to the longitudinal modulus of elasticity E_1 and the shear modulus G_{12}. A change in 5% in the shear modulus yielded a change in almost 20% in the energy absorbed by frame 2I-3. Finally, material properties given by different authors (Sensmeier et al., 1988; Collins et al., 1991; Tsai, 1992; Woodson, 1994; Moas, 1996), as listed in Table 2.1, are used as a data base to evaluate the influence of material property changes on the predicted the response of frame 2I-3. After many trial runs of the analysis code using different values for the intact lamina material properties, the values selected which give a reasonable correlation with the test are listed in column seven of Table 2.1. The results from the analysis using these selected values is shown in Fig. 2.2, along with the test results and the original analysis using the nominal values given in Woodson (1994). Note that the load-displacement curve from the analysis with clamped end conditions shown in Fig. 2.1 and the curve using material properties from Woodson (1994) in Fig. 2.2 are the same. The selected values for E_1 and G_{12} are low relative to the nominal values used for this material as given in columns three, five and six of Table 2.1.

2.3 Design of frames 2I-1, 5I-2, and 6I-2 for improved energy absorption

The values selected for the material properties from the correlation with the baseline frame 2I-3 as listed in Table 2.1 and clamped boundary conditions are specified in the design of frame 2I-1. The specified maximum crushing force F_{max} = 1500 lb, which is less than the 1800 lb maximum load from the test of the baseline frame. A parametric study is performed by reducing the width of the radially inboard flange, denoted by b_i, and reducing the width of the skin laminate, denoted by b_s, from the baseline values around the entire circumference. The range of the design variables considered is 1.0 in. < b_i < 1.50 in.

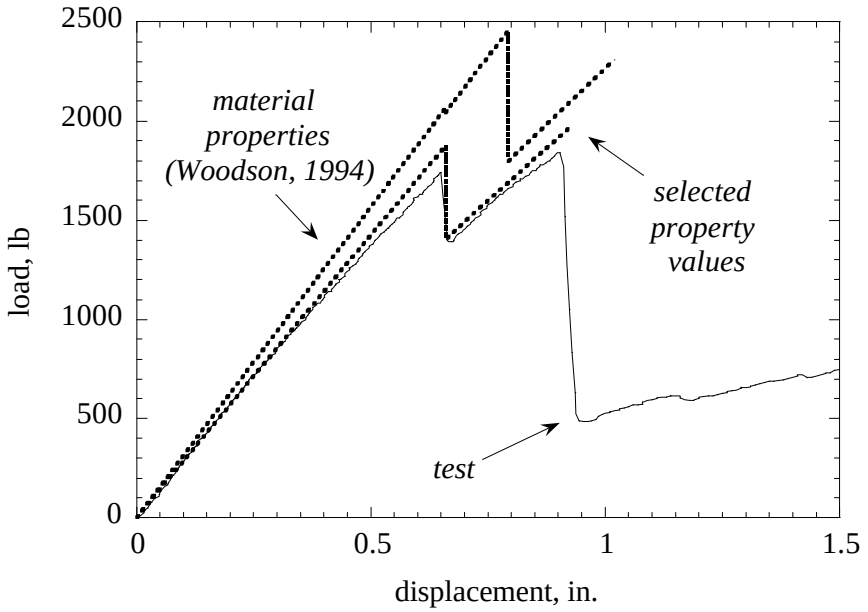

Fig. 2.2 Analytical results for different material properties.

and 2.5 in. < b_s < 3.5 in. The lower limit for b_s corresponds to the width of the radially outboard flange which is held fixed in the design. Initially, seven equally spaced values of each of the design variables is considered with a decrement of 10% of $(b_i)_{max}$. Convergence of the optimizer in this design space of only forty-nine possible designs gave no feasible designs. The best of these infeasible designs (the one with the largest fitness) is selected and the algorithm is repeated using seven new values for b_i and b_s within the ranges listed above but with an increment between values based on 10% of the new $(b_i)_{max}$. This process is repeated thirteen times until a feasible design is determined (one with no penalty to the fitness function). Thus, the number of designs considered is approximately 637. The dimensions for the optimal design are b_i = 1.048 in. and b_s = 2.506 in. with the energy absorbed E_a = 809.2 lb-in. The energy absorbed for the baseline frame up to the 1500 lb design load is 395.5 lb-in. Hence, there is a 105% increase in the energy absorbed by the redesigned frame compared to the baseline design. The total energy

absorbed and weight obtained from the analysis for both cases are summarized in Table 2.2, and the response curves are shown in Fig. 2.3.

Table 2.2 Analytical results for the original and redesigned frames.

frame	case	weight, lb	flange widths, in.		maximum specified load, lb	energy absorbed to the maximum specified load, lb-in.
			inner, b_i	skin, b_s		
FR002I-1	original	7.77	1.50	3.50	–	395.5[a]
	redesigned	6.47	1.05	2.50	1500.0	809.2
FR005I-2	original	7.49	1.50	3.50	–	244.4[a]
	redesigned	5.96	0.812	2.5	750.0	595.8
FR006I-2	original	7.55	1.50	3.5	–	196.3[a]
	redesigned	5.97	0.774	2.5	750.0	432.9

a. Energy absorbed in the original frame to the maximum specified load of the redesigned frame.

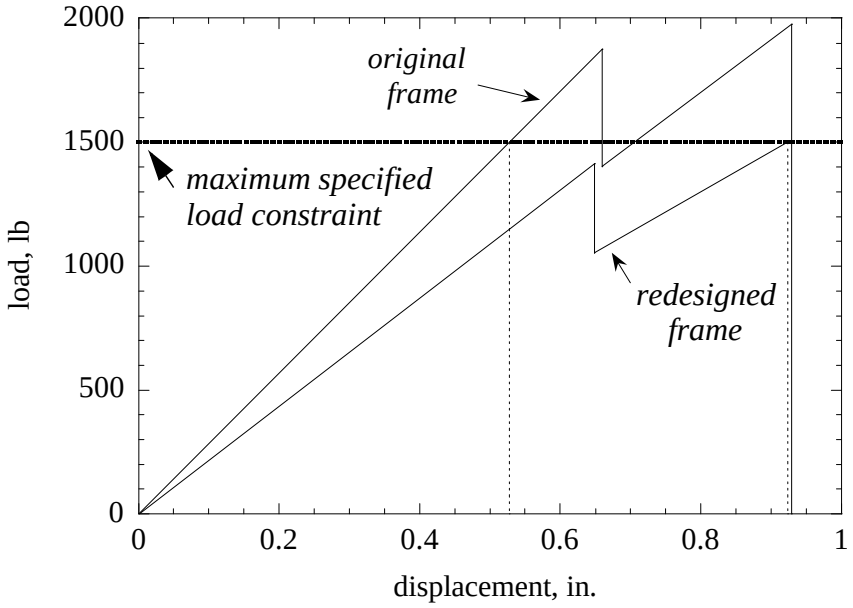

Fig. 2.3 Analytical results of the redesigned, and the original, baseline frames.

Buckling of the frame is a possibility, but the analysis does not account for structural instability. To determine if the redesigned frame would buckle prior to the first major fail-

ure event at 1500 lb, the buckling load from the stability code developed by Moas (1996) is computed. This stability code is implemented in the CSM Testbed (a structural analysis software system) at the NASA-Langley Research Center. The buckling load obtained from the stability code, 2139 lb, is larger than the maximum load predicted from the analysis, 1500 lb, so buckling prior to material degradation appears unlikely.

Frames 5I-2 and 6I-2 are redesigned for a design load of 750 lb using the same selected material properties used for frame 2I-1. The results obtained from the analysis for the original and redesigned frames are also listed in Table 2.2.

2.4 Test apparatus and procedure

A Baldwin servo-hydraulic testing machine with a maximum axial force capacity of 120000 lb is used to load the frame specimens. A frame mounted in the machine before testing is shown in Figure 2.4. A wide flange steel beam (W6 x 12) is bolted to the stationary crosshead in the testing machine to support the frame specimen (Moas, 1996). This steel beam is selected based on an analysis that the deflection of the beam under load would be less than one percent of the maximum deflection of the specimen.

The ends of the frames are secured to the wide flange beam through two steel blocks bolted to the flange of the beam. The steel blocks are 5 in. wide by 3.5 in. deep by 1.5 in. thick, and have slots machined in them in the shape of the I-section to receive the ends of the frames. The slots cut in the steel block provide approximately 0.1 in. of clearance between the block and the specimen, and this gap is filled with Hysol-934 potting compound. These end fixtures maximize the clamping rigidity by minimizing the amount of potting material used (Moas, 1996). The potting compound is mixed using 60% epoxy, 20% catalyst, and 20% glass beads by weight. The mixture is poured into the slot and the specimen is immediately inserted into the potting compound and held fixed until the mixture cures.

The frames are subjected to compression by moving the bottom table of the load frame upward in a displacement-controlled mode. The stroke of the test machine is limited to approximately 5 in., which is a sufficient stroke capacity in which to observe all major

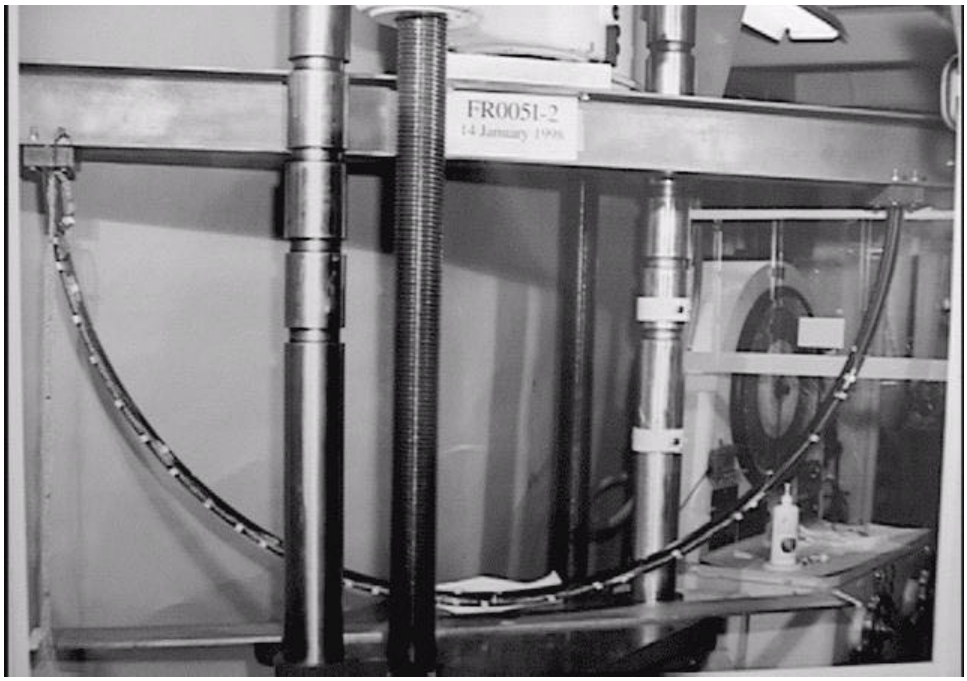

Fig. 2.4 A frame mounted in the test machine.

failure events of the frames. The tests are conducted such that the initial loading rate is 1000 lbs per minute. The data collected during the tests consists of the vertical force, vertical displacement, and strains. Uniaxial strain gages (0.187 in. gage length), and three-element strain gage rosettes (0.062 in. gage length) are bonded to the frames in several locations around the circumference. The analog data from the transducers are converted to digital form and recorded on a computer hard disk, and then plotted.

2.5 Test results of the redesigned frames

2.5.1 Frame 2I-1

The load-displacement curve, and circumferential surface strain distributions of frame 2I-1 are shown in Figs. 2.5, and 2.6. The load-displacement curve of frame 2I-1 is linear in the initial portion followed by a slight softening of the response. The first major failure event occurs at a load of 1962 lb and at a displacement of 1.19 in. This failure is due to a crack in the web near $q = 0°$. After attaining the maximum load of 1962 lb, a significant drop in the load is observed (from 1962 lb to 328.3 lb). As a result of this failure, the web and the inner flange are fractured (Fig. 2.7). This fracture results in the lateral movement

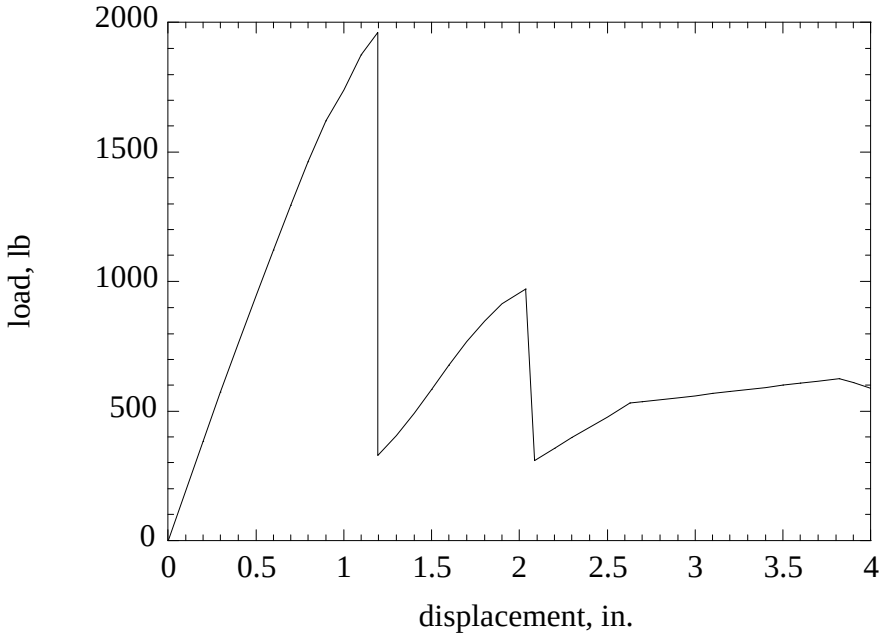

Fig. 2.5 Force-displacement response of frame 2I-1.

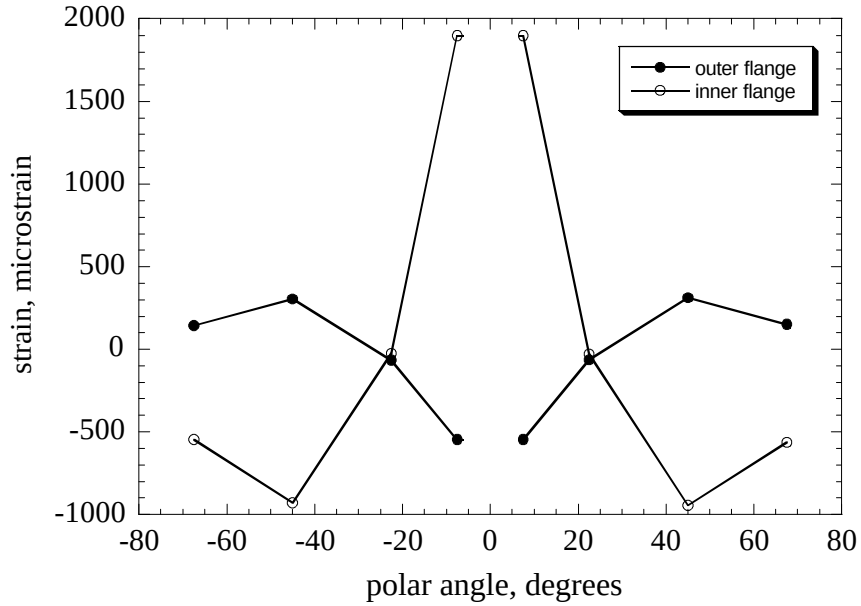

Fig. 2.6 Circumferential strain distributions on the flanges of frame 2I-1 at the first failure event.

of one side of the frame with respect to the other, causing the subsequent response to be unsymmetrical. As the test continues, a reloading at a stiffness lower than the initial stiff-

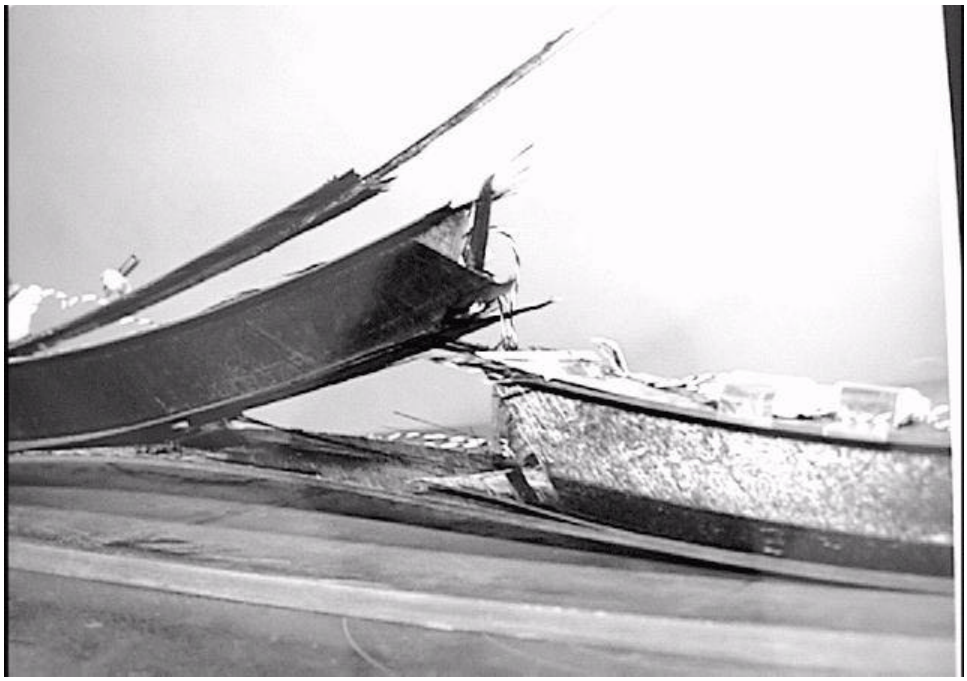

Fig. 2.7 The first major failure event of frame 2I-1 occurring at the point of load application (q = 0°).

ness takes place. One side of the frame begins to bend, creating a hinge near q = 45° from the center of the frame (Fig. 2.8). The side of the frame which develops the hinge failure is called side A. The other side, side B, remains intact when the hinge develops in side A. At a load of 971.6 lb and a displacement of 2.04 in., a crack in the interface between the web and the inner flange occurs at this location forty-two seconds after the first failure. There is another drop in the load and a subsequent reloading at a lower stiffness than before. Later, a crack in the outer flange develops at q = 45° at a load of 625.5 lb and a displacement of 3.82 in. This causes the total separation of the inner flange and the outer flange for an arc length of about 5° on both sides of the crack. After this event, delamination of the cap plies of the inner flange is also observed over an arc length of about 30° from the end of the frame. Side B of the frame remains basically intact. At the end of the test, delamination along the interface between the cap plies and the channel plies is observed in some portions along the arc length of the frame, particularly along the inner flange. (Refer to Fig. 1.4 on page 6.) In the outer flange, this delamination of the cap plies and channel plies primarily occurs close to the main failure event locations, near q = 0° and q = 45° on side B. In a less dramatic manner, this behavior is observed at both ends of the frame, near q =

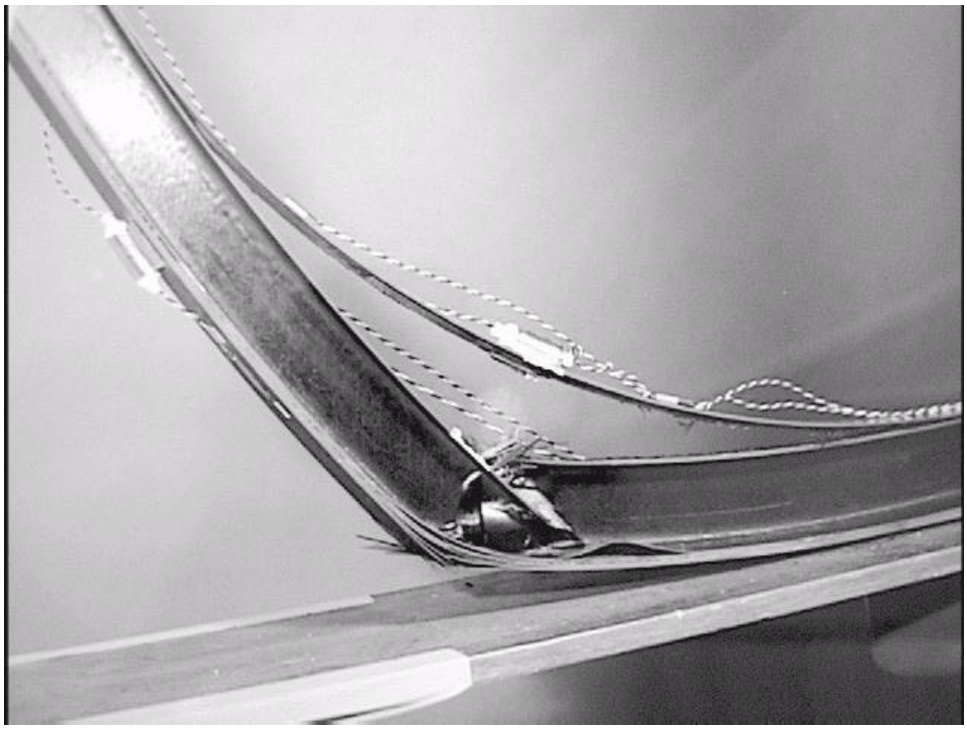

Fig. 2.8 The second major failure event of frame 2I-1 occurring near q = 45°.

± 90°. Also, some delamination in the web near q = 90° of side A is observed. Examination of the frame after the test revealed that a crack exists in the outer flange at q = 0°. Frame 2I-1 after the test is shown in Fig. 2.9.

The circumferential surface strains, shown in Fig. 2.6, attain relative maximums near q = 0° and q = 45° immediately prior to the first major failure event. The largest tensile circumferential strain occurs in the inner flange at q = 0°, and the largest compressive strain occurs in the outer flange at q = 0°. At the second critical location near q = 45° where the bending moment is of the opposite sense from its value at q = 0°, a compressive circumferential strain exists in the inner flange and a tensile circumferential strain exists in the outer flange.

2.5.2 Frame 6I-2

The load-displacement curve, and circumferential surface strain distributions of frame 6I-2 are shown in Figs. 2.10 and 2.11. The first major failure event occurs at a load of 1302 lb and a displacement of 1.95 in with a complete fracture of the web and the inner flange.

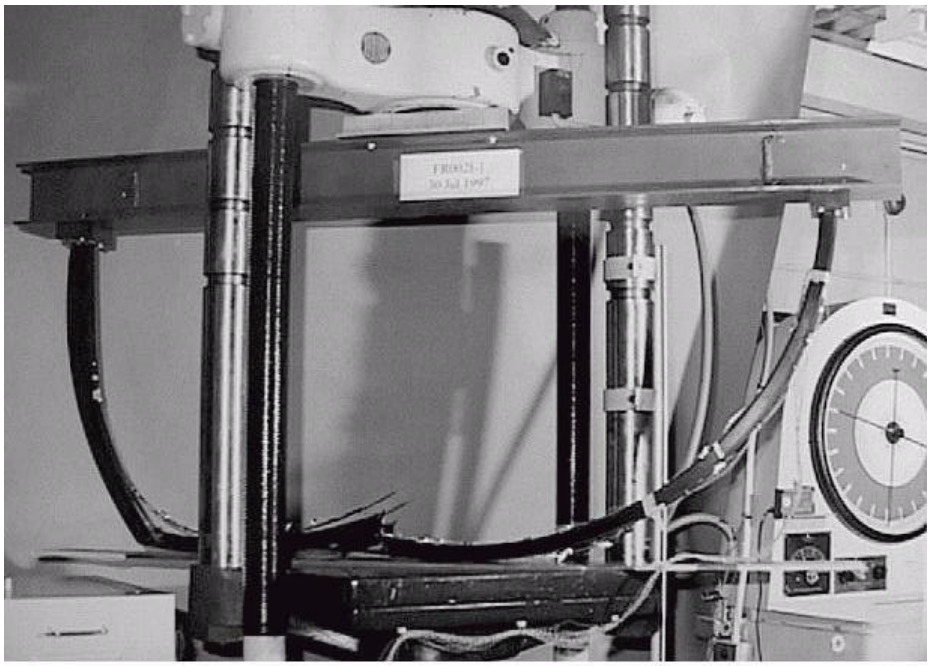

Fig. 2.9 Frame 2I-1 at the completion of the test.

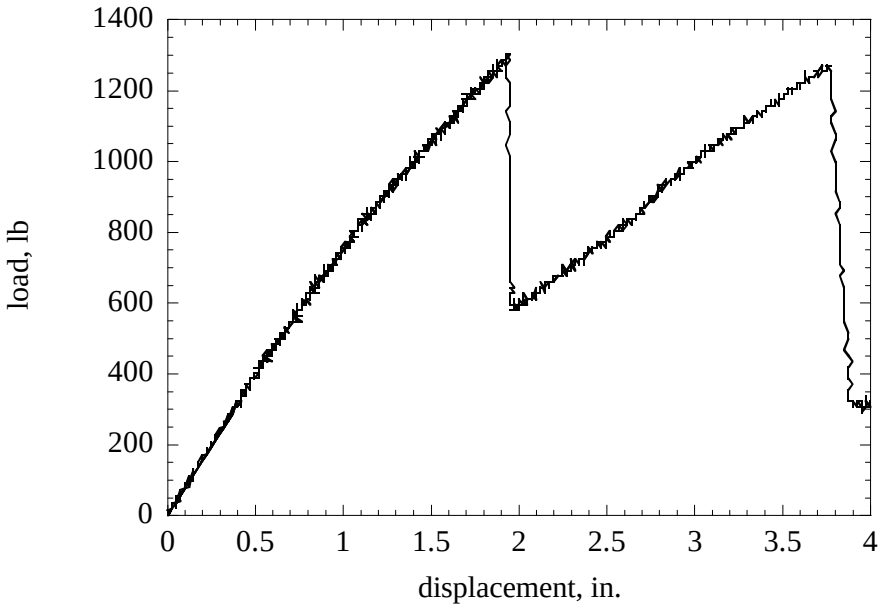

Fig. 2.10 Force-displacement response of frame 6I-2.

Delamination of the cap plies of the inner flange is observed for about 10° of arc length in the center of the frame. Also some delamination is present near q = 0° in the web and the outer flange. After the first failure event, the load drops to 580.1 lb. Then the load

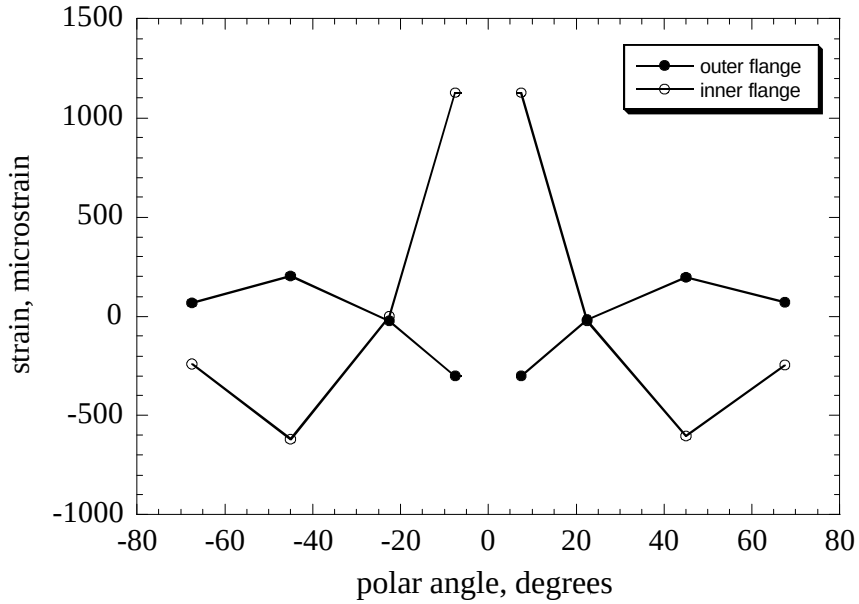

Fig. 2.11 Circumferential normal strain distribution on the flanges of frame 6I-2 at the first failure event.

increases again, but at a lower stiffness than the initial stiffness, until a load point of 1270 lb and 3.78 in. At 1270 lb the second major failure occurs, which is nearly the same magnitude as the load at the first major failure event. In fact, the energy absorbed between the first and the second failure events is larger than the energy absorbed to the first failure event. At the second failure event, the web/inner flange junction fails near $q = 45°$. Delamination and a fracture of the external plies of the outer flange is observed near this spanwise location. Delamination between the inner flange and the web develops in the same side of the frame that exhibits failures between 50° and 90°. As in the previous test, the other side of the frame remains basically intact (Fig. 2.12).

2.5.3 Frame 5I-2

The load-displacement curve, and circumferential surface strain distributions of frame 5I-2 are shown in Figs. 2.13, and 2.14. The load-displacement curve shows a single major failure event at a point of 1291 lb and 1.60 in. In this test, contrary to the previous ones, even though the web fractured, the external plies in the flanges do not fracture. This frame behaves more symmetrically than the other two after this first failure event. As the test continues, even though some delamination is observed in the web and flanges at both sides

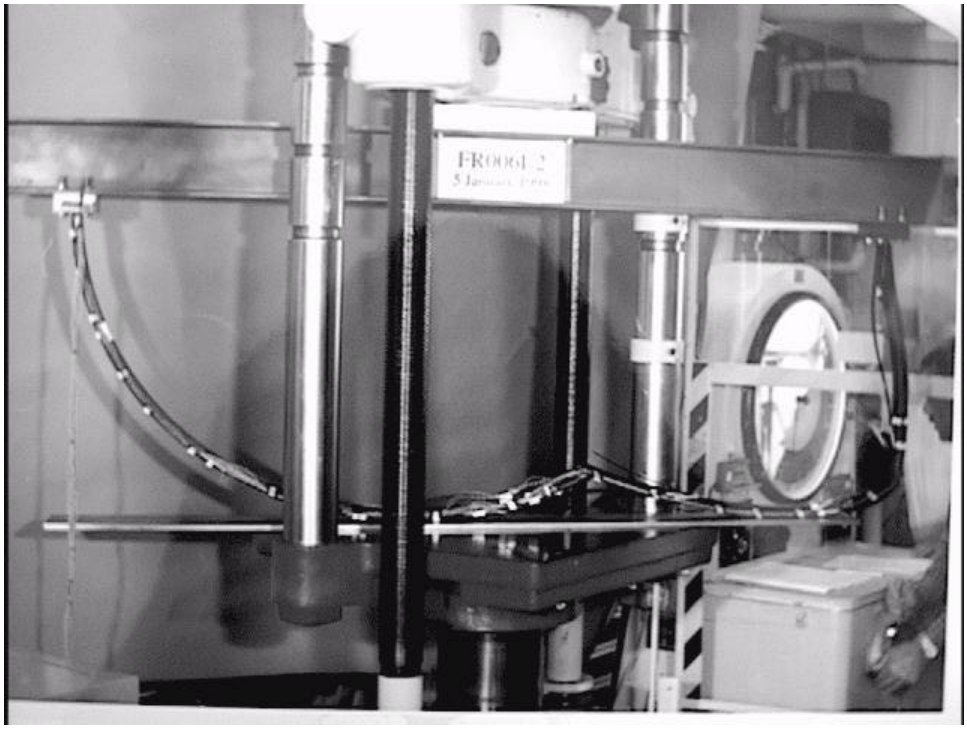

Fig. 2.12 Frame 6I-2 at the completion of the test.

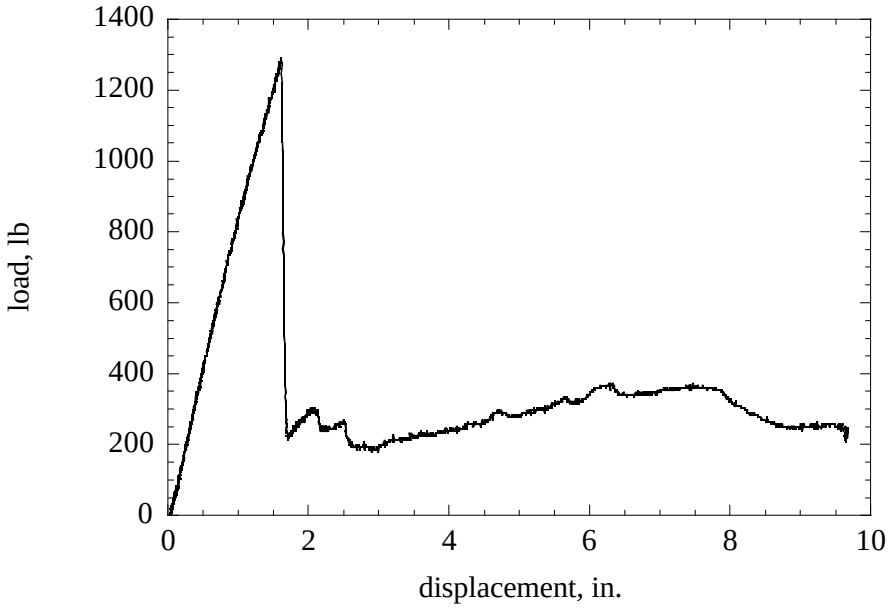

Fig. 2.13 Force-displacement response of frame 5I-2.

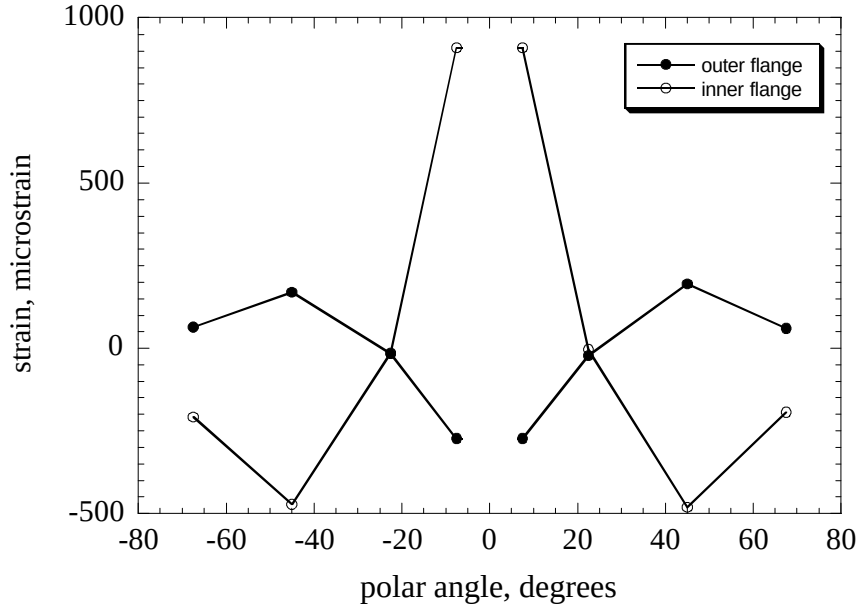

Fig. 2.14 Circumferential normal strain distribution on the flanges of frame 5I-2 at the first failure event.

of the frame near $q = \pm 45°$, the frame does not fail catastrophically in either side. For this reason we have just a single major failure event (Fig. 2.15). Some reloading is observed after this point, but at load levels lower than the previous failure. The fact that the inner flange delaminates from the web but otherwise remains intact, causes extensive delamination between the inner flange and the web along the span of the frame as the loading increased. This delamination extends about 50° from the center to both sides of the frame (i.e., about 100° total). Although delamination is extensive, the drop in the load, and the reduction in absorbed energy, associated with this visible delamination growth are small.

The circumferential surface strain distributions for frames 6I-2 and 5I-2, shown in Figs. 2.11 and 2.14, are those recorded immediately before the first failure event, which corresponds to displacements of 1.60 in. for 5I-2 and 1.95 in. for 6I-2. Even though frame 6I-2 absorbs about twice the energy as frame 5I-2, the circumferential surface strain distributions are relatively close in terms of magnitude, as are the test results up to the first major failure event. The circumferential strain distribution curves of these two frames are similar in shape to the distribution exhibited by frame 2I-1.

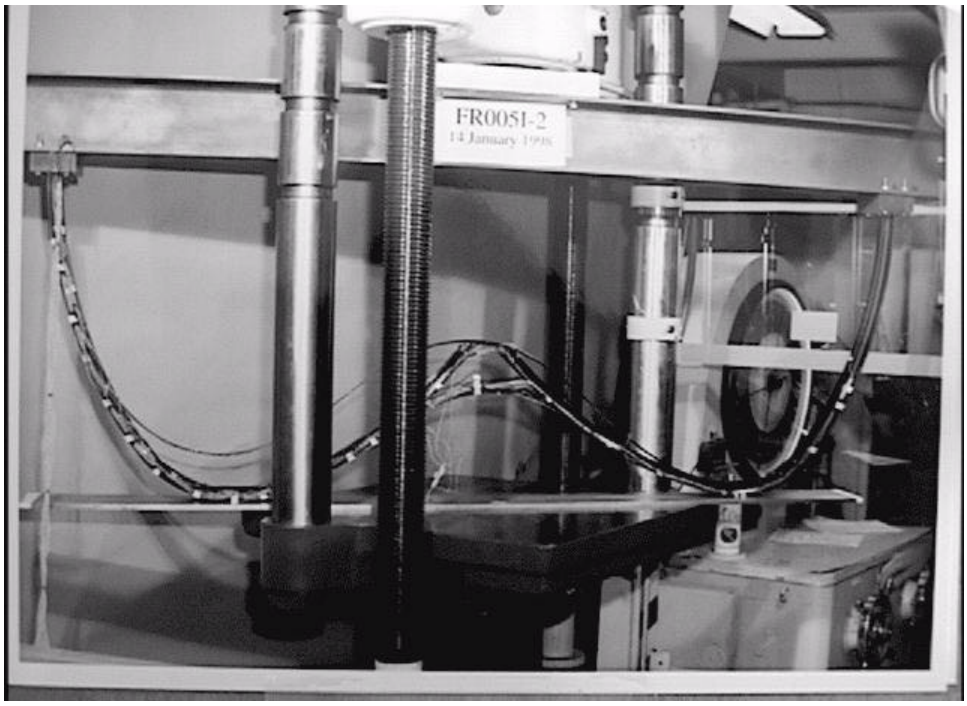

Fig. 2.15 Frame 5I-2 at the completion of the test.

2.6 Comparison of analyses and tests for the redesigned frames

The load-deflection curves from the analyses and tests of the baseline frame and the three redesigned frames are shown Figs. 2.16, 2.17, and 2.18. For each redesigned frame, the maximum loads in the tests are comparable in magnitude to their corresponding baseline test, instead of being close to the maximum specified load selected for each design. In other words, the maximum loads attained in the tests exceeded the maximum specified loads in all three cases studied. The frame stiffnesses in the tests are predicted very accurately by the analyses, as can be seen in the figures when comparing the test results with the analytical predictions. The load-displacement curve obtained from the analysis is in reasonable agreement with the test results up to the maximum specified load. Then, the test results show the load increasing to nearly the same maximum load as in the baseline frame (original) test. However, the reduction in the stiffness for these redesigned frames results in a larger amount of energy absorbed at the maximum specified load compared with their baseline tests counterparts. Energy absorption values up to the design load for each case are listed in Table 2.2. Energy absorption up to the first failure event is also

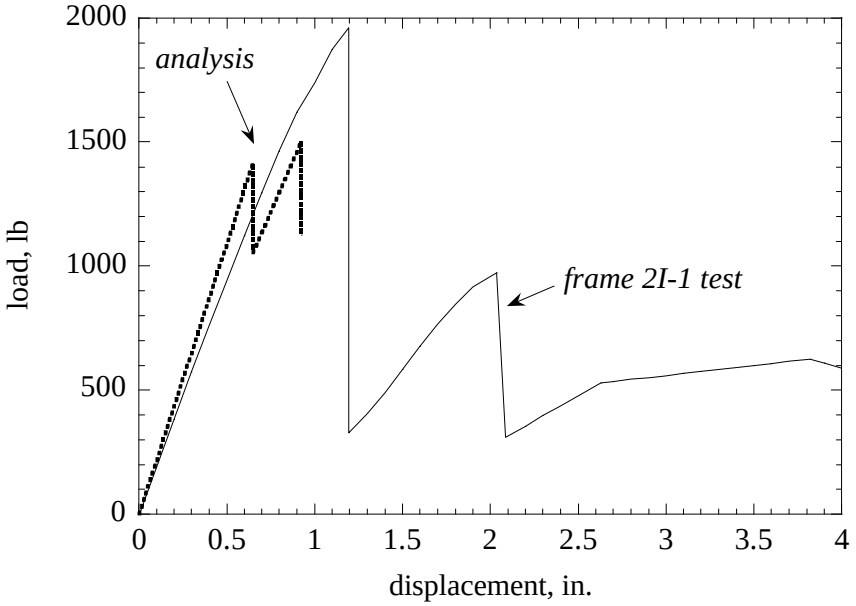

Fig. 2.16 Analysis and test results for the response of frame 2I-1.

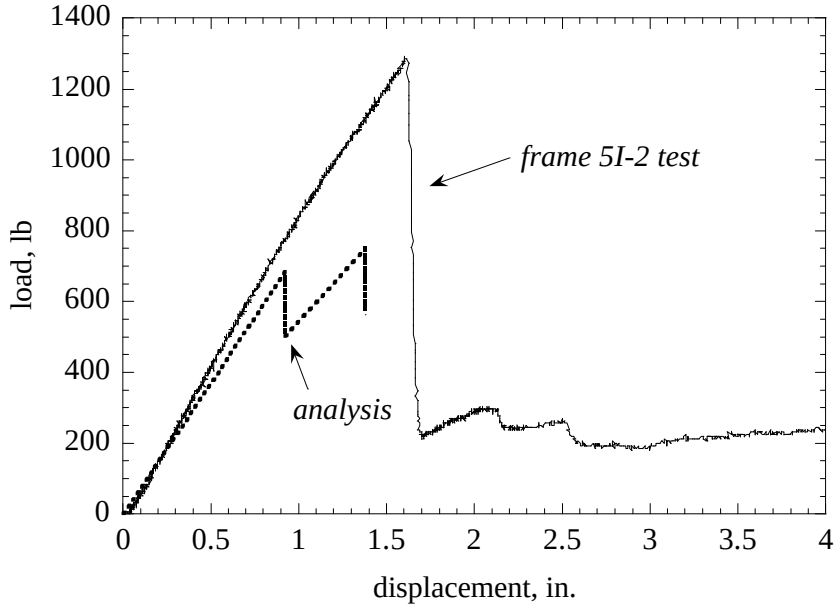

Fig. 2.17 Analysis and test results for the response of frame 5I-2.

included. These results show that reducing the flange widths reduces the stiffness of the frame, but the flange width reduction does not have a dramatic effect on the maximum load with respect to the baseline (original) cases.

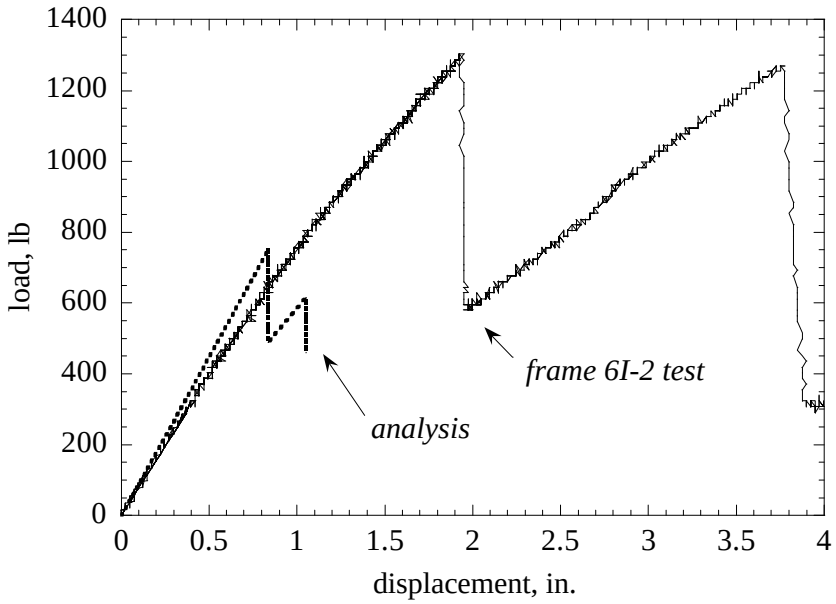

Fig. 2.18 Analysis and test results for the response of frame 6I-2.

In the analysis code, the applied load is modeled as a radially inward displacement at the apex of the frame. At the beginning of the analysis, an initial displacement is arbitrarily prescribed, and its computer value at the first failure event is the initial value times the minimum strength ratio (Woodson et al., 1996). To simulate actual test conditions, the displacement at the second failure event must be larger than the displacement at the first failure, the third must be larger than the second, and so on. If the displacement at the next failure in the sequence is smaller than the displacement at the previous failure, the process of failure and material degradation is continued until a displacement larger than the displacement at previous failure is found. If this does not happen, the analysis will stop when all lamina have failed in the fiber mode. As shown in Figs. 2.16 to 2.18, the results from the analysis show two major failure events, both relatively close in terms of the displacement. The failure sequence predicted by the analysis for frame 2I-1 is shown in Fig. 2.19. After the first failure event, labeled as *1*, there are four failures; the one labeled as *2* is considered the second failure event because its displacement is the only one that is higher than the displacement of the first failure event. In the analysis, every ply is assigned an identification number. The ply identification numbers for the model of frame 2I-1 are

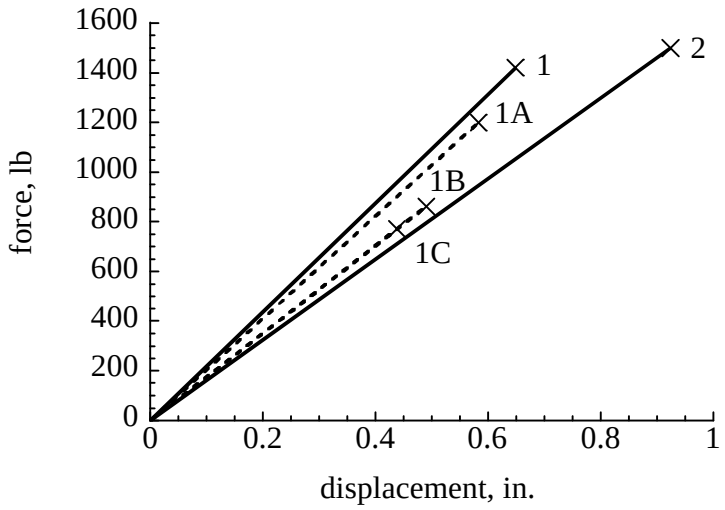

Fig. 2.19 Failure analysis for frame 2I-1.

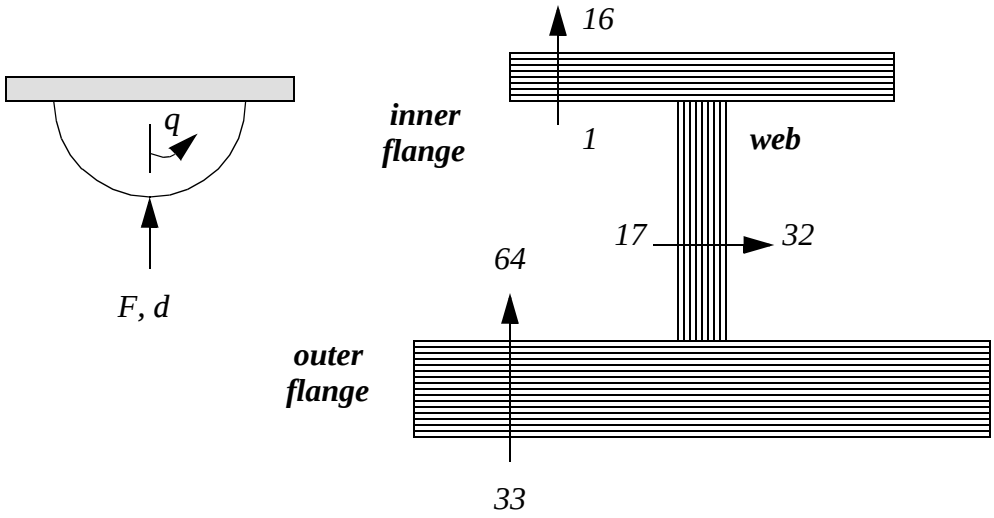

Fig. 2.20 Identification number of the plies in the cross-section of the PROFAIL model of frame 2I-1.

shown in Fig. 2.20; plies 1 to 16 constitute the inner flange, plies 17 to 32 constitute the web, and plies 33 to 64 are the plies of the skin and the outer flange.

The failure sequence and locations predicted by PROFAIL for frame 2I-1 are shown in Table 2.3. According to the analysis, the first failure event begins at a load of 1420 lb, and occurs in the 0°-plies of the inner flange and the web, at the center of the frame (q = 0°).

The plies fail first in matrix mode and then in fiber mode (a substantial reduction in laminar stiffnesses accompany the fiber failure mode, so the lamina has negligible load-carrying capability). The location of this failure agrees with the results of the tests. Even though it is not possible to know exactly what plies are failing during the test, it was observed that the first failure event began in the web/inner flange interface near the center of the frame. The second failure event begins at a load of 1500 lb, and occurs simultaneously in the 90°-plies of the web and the inner flange, near $q = 45°$ (matrix failure) and $q = 0°$ (fiber failure). This also agrees with the results of the tests. During the test, a hinge develops at about $q = 45°$, and a crack is seen in the web/inner flange interface. Nevertheless, the load and displacement corresponding to these failure events in the tests do not agree with the prediction.

The tests results from the redesigned graphite-epoxy frames 2I-1, 5I-2, and 6I-2 show an improved energy absorption relative to their original counterparts. The mathematical model for the optimal design and analysis of the frames predicts the correct sequence and location of failure events. However, the maximum specified loads for the redesigned frames were exceeded in the tests. Hence, the mathematical model does not predict the correct magnitudes of the force and displacement at the first major failure event. The reason for this could be related to the limitations of the analysis. For example, the analysis is geometrically linear. In addition, the cross-section is assumed to be rigid in its own plane (no curling of the flanges). The analysis does not consider local load distribution due to contact, nor interlaminar failure modes.

Table 2.3 Failure sequence and locations for frame 2I-1 predicted using PROFAIL.

failure	load, lb	displacement, in.	type of failure	id numbers of the plies that are failing[a]	polar angle, degrees
1	1420	0.649	matrix	3 (0°) 6 (0°) 11 (0°) 19 (0°) 27 (0°) 30 (0°)	0°
1A	1270	0.583	fiber	3 (0°) 6 (0°) 11 (0°) 19 (0°) 27 (0°) 30 (0°)	0°
1B	862	0.490	matrix	14 (0°)	0°
1C	771	0.438	fiber	14 (0°)	0°
2	1500	0.924	matrix	4 (90°) 5 (90°) 20 (90°) 21 (90°) 28 (90°) 29 (90°)	45°
2	1500	0.924	fiber	4 (90°) 5 (90°) 12 (90°) 13 (90°) 20 (90°) 21 (90°) 28 (90°) 29 (90°)	0°

a. Refer to Fig. 2.20.